applied sciences

MDPI

*Article*

# Less Rare-Earth Electromagnetic Design for a High-Performance Permanent Magnet Motor

**Christian A. Rivera *, Gaizka Ugalde, Javier Poza, Fernando Garramiola and Xabier Badiola**

Faculty of Engineering, Mondragon Unibertsitatea, 20500 Mondragon, Spain; gugalde@mondragon.edu (G.U.); jpoza@mondragon.edu (J.P.); fgarramiola@mondragon.edu (F.G.); xbadiola@mondragon.edu (X.B.)
* Correspondence: carivera@mondragon.edu

**Abstract:** This paper presents an electromagnetic design alternative using the so-called banana-shaped magnets, achieving magnet weight reduction of 21.82% for the same performance as the baseline motor in the case study. Typically, parallel magnetization is used in this topology because it provides the manufacturing advantage of not building a specific magnetizing device required to achieve radial magnetization. Therefore, as its main contribution, this paper proposes using tilted magnetization, demonstrating that the performance is better than the conventional way of applying parallel magnetization in banana-shaped motors but still using parallel magnetization. Because of the performance improvement for the same motor structure, magnet weight reduction is possible for a new design with the same performance as the baseline motor. In addition, this paper presents the workflow followed to obtain the less rare-earth design motor candidate using tilted magnetization.

**Keywords:** electric motor design; electromobility; less rare-earth; permanent magnet motor design; parallel magnetization; tilted magnetization



**Citation:** Rivera, C.A.; Ugalde, G.; Poza, J.; Garramiola, F.; Badiola, X. Less Rare-Earth Electromagnetic Design for a High-Performance Permanent Magnet Motor. *Appl. Sci.* **2022**, *12*, 3736. https://doi.org/10.3390/app12083736

Academic Editor: Youngmin Kang

Received: 23 February 2022
Accepted: 5 April 2022
Published: 7 April 2022

**Publisher's Note:** MDPI stays neutral with regard to jurisdictional claims in published maps and institutional affiliations.



## 1. Introduction

The reduction of $CO_2$ emissions policies has created a significant investment in transitioning fossil fuel vehicles to electric or minimizing fuel consumption with hybrid technologies. Although alternatives such as reluctance and induction machines could be possible, the electromobility (e-mobility) industry still relies on permanent magnet (PM) motors due to their higher efficiency and power density. Therefore, the implementation of rare earth elements (REEs) is typical for high-performance machines. Moreover, since 2011, western countries have declared REEs critical raw materials because of the risk in supply from China. In addition, the expected growth in sales of electric vehicles (EVs) [1] and the implementation of REEs in other applications will create a significant demand for REEs [2], in particular for Neodymium. For this reason, there is a need to look for electric motor design alternatives that can eliminate or reduce REEs. This paper's interest is on the latter.

The design feature in this paper is the topological advantage the so-called banana-shaped (also known as crescent-shaped or arc-shaped) magnet geometry provides to the magnetic structure of the motor. Kim et al. [3] findings show that although they have the same magnet weight, the electromotive force of the motors with arced magnets is higher than the block types analyzed. Hayakawa et al. [4] compare the three-layer V-shaped structure with the three-layer arc-shaped structure, resulting in higher torque for the latter because of a better ratio of magnet and reluctance torque. Similarly, Abad et al. [5] state that the double-layer arced structure required the least magnet material compared to the conventional block type structures to achieve the targeted performance. Their work [3–5] demonstrates that the arc-shaped structure provides the advantage of efficient use of the magnet material compared to the block type. Therefore, opening the possibility of less rare-earth designs.

From the literature, it is noticeable that few scientific publications have addressed this issue and those that have, made the study with either neobonded or ferrite magnets. However, the interest of this research is on Neodymium-Iron-Boron (NdFeB), the typical structure for high-energy PM. Compared with other technologies (Alnico, Ferrite, Samarium-Cobalt), NdFeB magnets provide advantages such as higher coercivity and higher magnetic flux density remanence. In addition, the addition of Dysprosium and Terbium (heavy RE) enhances the thermal stability properties of these magnets.

Moreover, NdFeB magnets with these complex shapes have manufacturing difficulties for mass production. One reason is that taking the conventional production route for sintered magnets requires cutting, leading to significant scrap. This material waste could be a reason for the lack of studies on NdFeB sintered magnets with arc shapes. However, new manufacturing technologies, such as additive manufacturing or Powder Injection Molding (PIM), can potentially implement these geometries on sintered magnets for mass production shortly. For instance, nowadays, there are commercial ring-shaped examples of sintered NdFeB [6]. Therefore, studying this type of topologies in electric motor design is attractive. Although magnet manufacturing-specific details are out of the scope of this paper, it should be mentioned that this work is part of the European LowRee Motors project [7] founded by EIT raw materials, where new magnet manufacturing processes are studied (PIM and Cerium substitution) for rare-earth reduction. So, for this reason, the banana-shaped topology is selected as a complex shape magnet that could be developed through PIM. The study presented in this paper intends to check before implementing a specific manufacturing process if rare-earth reduction could be achieved for this topology through electromagnetic design only, taking a baseline motor as the starting point.

The most applied magnetization patterns in the design of electric motors are parallel and radial magnetization. The literature shows interest in the study of magnetization patterns [8]. There are many studies regarding surface permanent magnet motors (SPM) [9–15], including Halbach magnetization for this type. Each pattern has its pros and cons, but results usually show that radial magnetization leads to higher torque values regardless of the magnet material. Similarly, we can find few studies for banana-shaped Interior Permanent magnet Motors (IPM). These references [3–5,16–18] present studies that demonstrate an improvement in mean torque with this topology. Kim et al. [3,16,17] studies show different performances are obtained by adjusting the radial direction, which they execute by changing the radius value of the center of magnetization in the molds used. The results in [4,5] show that these topologies increase the mean torque compared to conventional shapes. Abad et al. [5] radial magnetization application leads to a 6% torque increment than parallel.

However, despite the fact that radial magnetization provides the advantage of torque increment, its implementation in the industry has been limited due to its complexity and investment. The reason is that to accomplish it requires the specific adoption of a magnetizing device with molds for a component (part by part) or sub-assembly magnetization [19,20]. Post-assembly magnetization in the rotor could be another option for achieving a desirable radial magnetization pattern. Nonetheless, this process will also require an analysis to check if the stator windings can withstand the magnetizing current because if not, the magnet's magnetization will be lower [21,22]. Accordingly, creating the need to build a specific magnetizing device to achieve the required remanence.

Typically, for NdFeB, the industry follows the component magnetization manufacturing process [19]. The manufacturing process will require an extra investment for radial magnetization, increasing the unit cost of the magnets [5,13]. So, the slight torque improvement range (3–6%) compared to parallel magnetization might not compensate for the extra investment. Nevertheless, this torque loss due to parallel magnetization affects the effective usage of the implemented magnet weight in a motor. Thus, the question that arises is how to improve the performance of the banana-shaped motor with parallel magnetization for the effective use of the magnet weight. Effective use of the magnet weight will lead to savings in magnet material, and therefore, less rare-earth.

This article proposes an innovative magnetization pattern alternative for banana-shaped magnets that maintains the unit manufacturing cost of the conventional parallel magnetization (presuming the existence of a baseline motor already using parallel magnetization) but increases the motor performance for the same magnet weight. This magnetization pattern proposal is the so-called tilted magnetization that consists of the optimal magnetization angle for the magnets. This optimal angle is found through finite element method (FEM) analysis demonstrating it produces a better motor performance for the baseline motor. To the authors' understanding, this fact has not been reported, making it the contribution of this paper. Therefore, since the proposed tilted magnetization pattern improves the baseline banana-shaped motor performance, it also opens the possibility to achieve a new design considering the optimal use of magnet weight.

In summary, this paper presents a new electromagnetic design solution using tilted magnetization that could enable the mass production of banana-shaped NdFeB magnets with new manufacturing techniques such as the PIM technique keeping the unit cost as with the typical application of conventional parallel magnetization. Previous studies have already compared this type of motor with block-type motors; therefore, the scope of this paper is the electromagnetic design improvement through tilted magnetization for the same motor topology.

Therefore, the paper structure is the following. Section 2 introduces the baseline motor and requirements. Then, Section 3 evaluates the magnetization pattern and proposes the alternative tilted magnetization. Next, Section 4 proposes an optimization workflow using tilted magnetization. Section 5 discusses the results. Finally, Section 6 concludes the work and shares future work.

## 2. Baseline Electric Motor and Requirements

This section introduces the baseline electric motor. First, a short description of the models used in the analysis is described, followed by the requirements for the less rare-earth motor design candidate.

### 2.1. Baseline Motor—Electromagnetic and Thermal Models

The starting point is a built EV motor prototype designed by Li [23] consisting of five pole pairs, shown in Figure 1. Initially, the design was developed with Neobonded magnets with parallel magnetization. However, for our case study, the magnets were substituted in the electromagnetic model with NdFeB magnets having a remanence ($B_r$) of 1.1424 T and a relative permeability ($\mu_r$) of 1.018 at room temperature. The reason for choosing this $B_r$ and $\mu_r$ is to have a value that new technologies could reach under analysis in the LowRee Motors project, e.g., PIM and Cerium substitution. Therefore, for future work analysis.

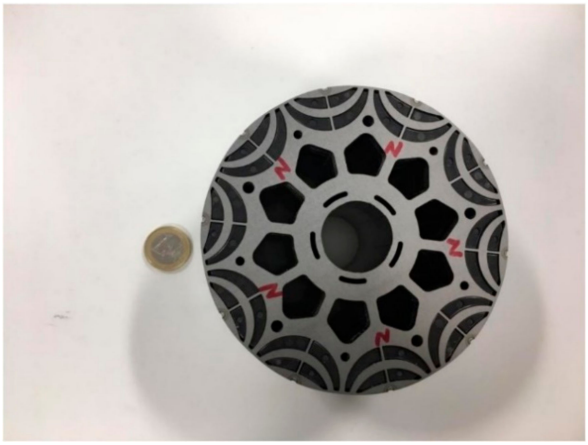

**Figure 1.** Baseline Motor designed reproduced with permission from [23], Ziwei Li, 2019.

The 2D electromagnetic model is developed in the FEM analysis software Altair Flux version 2020.1. Table 1 shows the parameters of the baseline motor electromagnetic model. It can be seen that the slot-pole combination would permit simulating one pole pair. However, because the holes between each pole are asymmetric, as seen in Figure 1, one pole pair has been simulated to consider their electromagnetic effect.

**Table 1.** Baseline motor electromagnetic model parameters.

| Parameter | Unit | Value |
|---|---|---|
| Outer diameter | mm | 161 |
| Stack length | mm | 66 |
| Number of slots | - | 60 |
| Pole pairs | - | 5 |
| Type of application | - | Transient magnetic 2D |
| Iron losses | - | Modified Bertotti model |
| Magnet Type | - | NdFeB |
| Magnet remanence | | 1.1424 T @ 20 °C |
| Magnet relative permeability | | 1.018 |
| Magnetization type | | Parallel magnetization |

The electromagnetic model type of application is transient magnetic 2D. This option was selected to compute iron losses using the modified Bertotti model applied in the magnetic materials in the same FEM software tool. The performance comparison is computed on the Maximum Ampere per Torque (MTPA) curve for the operating points. Previously developed FEM-coupled algorithms [24] are employed to do so. All performance results presented in this paper apply the same post-process methods using the equivalent circuits shown in Figures 2 and 3. The resistance $R_s$ account design changes by a modified Hanselman [25] equation adjusted from the measured resistance value from the baseline motor. The iron losses resistance $R_{fe}$ is derived from the power losses obtained in FEM, the losses are multiplied by an empirical factor to account for their increase due to pulse-width modulation. Similarly, the lamination stacking factor is considered in the performance computation. In addition, mechanical losses and end-winding inductance are considered in the post-process. The fluxes are obtained from FEM.

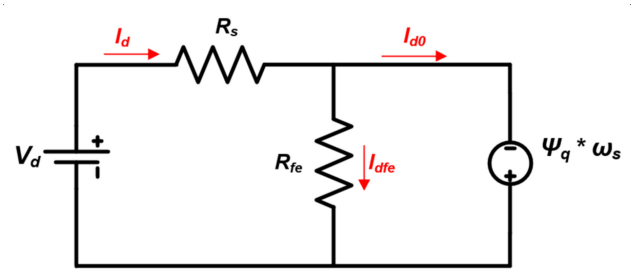


**Figure 2.** d–axis equivalent circuit.

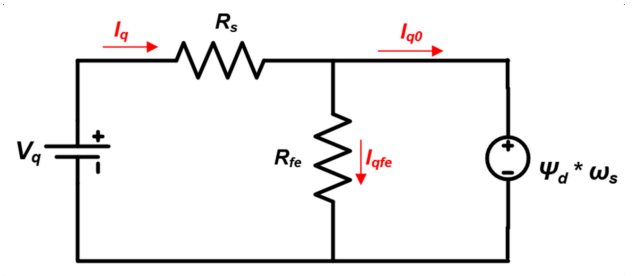


**Figure 3.** q–axis equivalent circuit.

Materials, winding details, exact geometric dimensions and empirical factors not included in the paper are confidential. The 2D view of the electromagnetic model is presented in Figure 4.

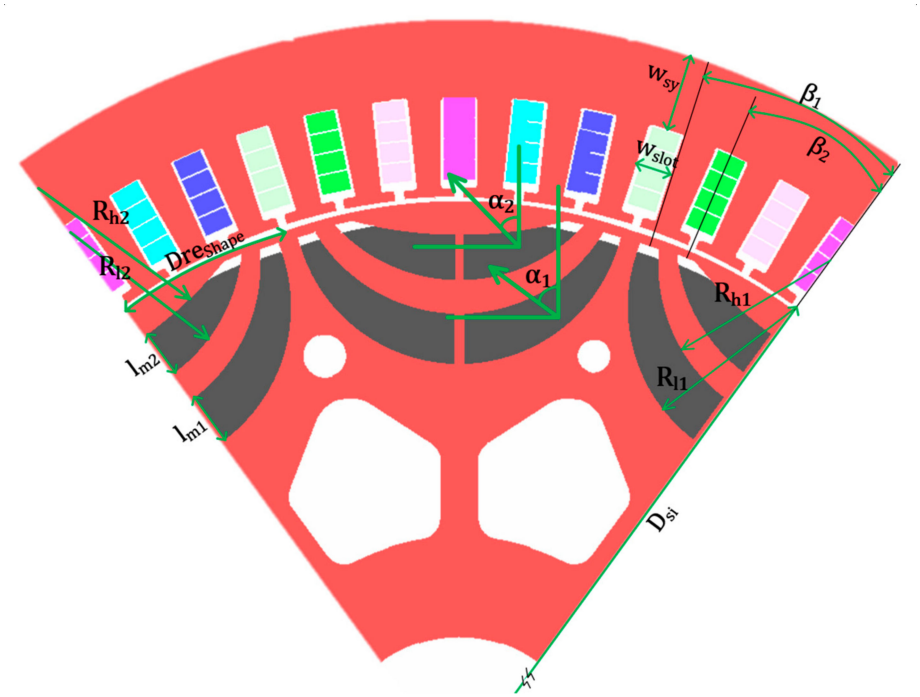


**Figure 4.** Baseline motor electromagnetic model and parameters.

Figure 5 shows the thermal model developed using the software ANSYS Motor-CAD version 13.1.11. Table 2 summarizes relevant information about the model. The cooling system of the baseline motor consists of a water jacket having one circumferential cooling channel over the stator. The front end-cap is closed, while the rear end-cap has open slots, also considered in the model.

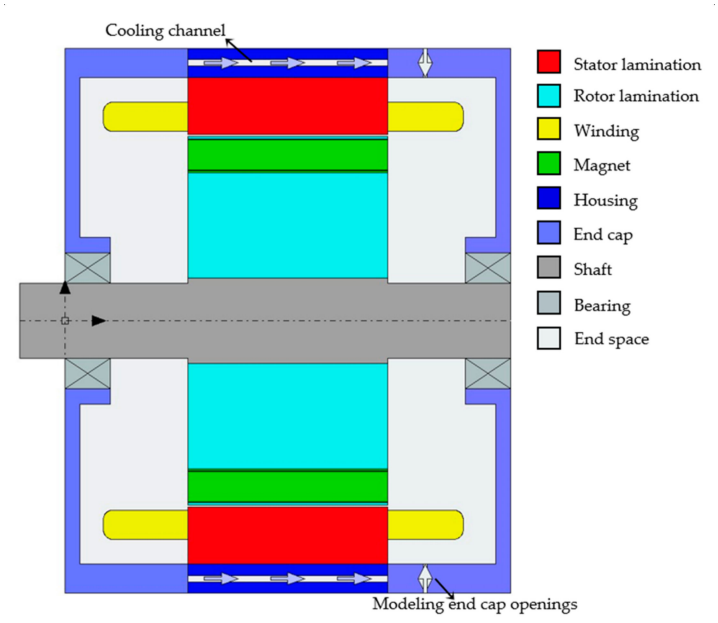


**Figure 5.** Baseline motor thermal model.

**Table 2.** Baseline motor thermal model parameters.

| Parameter | Unit | Value |
|---|---|---|
| Coolant | - | Water |
| Number of channels | - | 1 |
| Flow rate | L/min | 6 |
| Inlet temperature | °C | 80 |

### 2.2. Less Rare-Earth Design Requirements

The focus for the performance study is on the motor's continuous torque at base speed, shown in Table 3. The requirements are also shown in the same table. The goal is to keep the same performance of the motor in terms of the same output torque at the same speed for the same thermal performance (same winding and magnet temperature). However, minimizing the magnet weight ($W_m$) with a lower torque ripple ($\tau_{ripple}$) if possible. Geometrically the motor is limited to the same outer diameter, same or lower stack length and the same slots-poles combination.

**Table 3.** Baseline motor performance and new design requirements.

| Parameter | Unit | Baseline Motor Performance | Requirement |
|---|---|---|---|
| Mechanical Torque | Nm | 39.34 | =39.34 |
| Speed | RPM | 2400 | =2400 |
| Torque ripple | % | 6.7 | $\leq$6.7 |
| Efficiency | % | 93.11 | $\geq$93.11 |
| Winding temperature | °C | 133 | ~133 |
| Magnet temperature | °C | 100.3 | ~100.3 |
| Magnet weight | kg | 1.3098 | Minimum |
| Outer diameter | mm | 161 | =161 |
| Stack length | mm | 66 | $\leq$66 |
| Number of slots | - | 60 | =60 |
| Pole pairs | - | 5 | =5 |

## 3. Proposed Magnetization Pattern for Banana-Shaped Magnets with Parallel Magnetization

Section 1 reviewed the banana-shaped magnets in motor design in terms of other shapes comparisons and magnetization. Hayakawa et al. [4], Kim et al. [3] and Abad et al. [5] compared this arced topology with block-type magnets. From their work, aside from the spoke topology, it can be concluded that this kind of topology allows more magnet material to be inserted than the block type. Usually, the insertion of more magnet material results in higher air gap magnetic flux density ($\hat{B}_g$) values, therefore increasing the PM torque component. Moreover, even if the same magnet weight is used, their work demonstrates that the arced topology increases the reluctance torque component.

Nonetheless, regardless of the motor's magnet topology, the air gap flux density decreases once it passes the maximum magnet length point for a fixed rotor structure. Figure 6 illustrates this behavior for a radial magnetized single-layer banana-shaped magnet at no-load operation. The curve in the figure shows the results obtained directly from FEM. The magnet length ($l_m$) is varied from one millimeter to sixteen millimeters and the peak flux density fundamental harmonic ($\hat{B}_{g1}$) value is extracted for each simulation. It can be noticed that once $\hat{B}_{g1}$ reaches its maximum limit, increasing $l_m$ does not increase $\hat{B}_{g1}$. However, it increases the magnet reluctance, which has more influence on the magnetic circuit. So, an effective tradeoff between $l_m$ and $\hat{B}_{g1}$ should be considered.

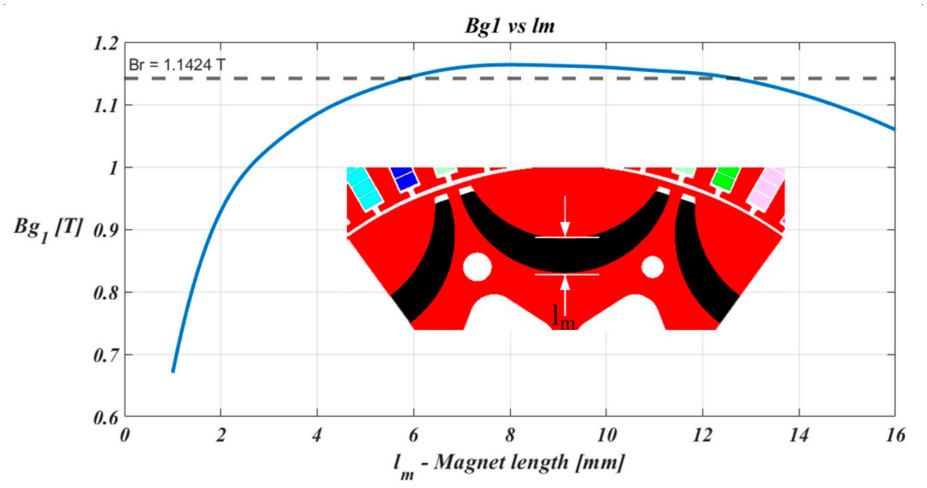


**Figure 6.** Fundamental harmonic air gap flux density vs. magnet length.

Moreover, this topology offers flux concentration capability that depends on the implemented magnetization. Equation (1) shows the well-known analytical relation to computing $\hat{B}_g$ without accounting for leakage [25]. Equation (1) is shown only to highlight that the $\hat{B}_g$ is affected by the magnet and air gap surface ratio (i.e., Equation (1) is not used to compute any result, all results are obtained directly from FEM). This ratio is the flux concentration factor ($C_{\varphi S}$), separated in Equation (2). The origin of this ratio is no other than saying that the flux leaving the magnet is equal to the flux crossing the air gap [25]. Therefore, one of the advantages of IPM machines with flux concentration techniques is the possibility of having a $C_{\varphi S}$ greater than 1.

$$\hat{B}_g = \frac{B_r}{1 + \mu_r \frac{S_m}{S_g} \frac{g}{l_m}} \frac{S_m}{S_g} [T] \tag{1}$$

$$C_{\varphi S} = \frac{S_m}{S_g} \tag{2}$$

Table 4 shows the magnet properties and the surface areas of the air gap ($S_m$) and magnet ($S_g$) for the single-banana case of Figure 7. So, applying Equation (2) in this specific geometric case tells us that the ideal maximum attainable $C_{\varphi S}$ is 1.2613 (see Figure 7).

**Table 4.** Surface areas and magnetic properties of a single banana layer simulation.

| Parameter | Unit | Parallel Magnetization | Radial Magnetization |
|---|---|---|---|
| $S_m$ | $mm^2$ | 2669.568 | |
| $S_g$ | $mm^2$ | 2116.587 | |
| $C_{\varphi S}$ | - | 1.2613 | 1.2613 |
| $B_m$ | T | 1.0336 | 0.9448 |
| $H_m$ | kA/m | 85.480 | 154.439 |
| $\hat{B}_g$ | T | 0.8740 | 1.0733 |
| $\hat{B}_{g1}$ | T | 0.9631 | 1.1354 |
| $C_{\varphi B}$ | - | 0.8456 | 1.1360 |
| $B_r$ | T | 1.1424 | 1.1424 |
| $\mu_r$ | - | 1.0180 | 1.0180 |
| $PC$ | - | 9.6712 | 4.8690 |

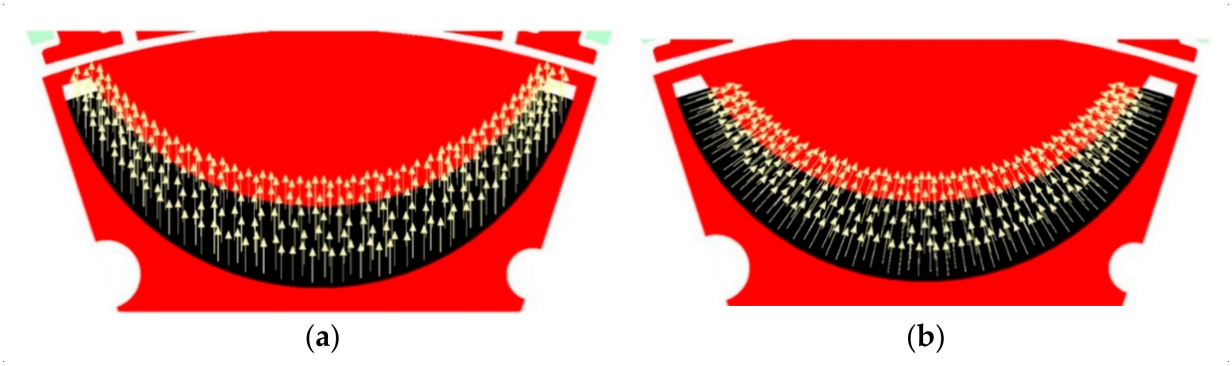


**Figure 7.** (**a**) Parallel magnetization; (**b**) Radial magnetization.

However, it is possible to account for the magnetization pattern and leakage by computing the flux concentration factor using Equation (3) if these flux density values are obtained directly from FEM. $B_m$ is the magnet operating point calculated as the mean value of the magnet's flux density distribution (same is done for the magnetic field: $H_m$). So, to check the difference, radial and parallel magnetization is applied as shown in Figure 7 and $\hat{B}_g$ and $B_m$ are obtained from FEM. The no-load simulation yields the results presented in Table 4. On the one hand, as expected, the results show that radial magnetization makes better use of the magnet weight for the same rotor structure, having a 9.93% decrease with the maximum attainable flux concentration factor. However, on the other hand, parallel magnetization decreased 32.95%, which translates into 17.89% less air gap flux density than the radial case. However, the permeance coefficient ($PC$) [25] (shown in Table 4) shows that radial magnetization leads to a lower magnet open circuit operating point than the parallel case, which could affect demagnetization.

$$C_{\varphi_B} = \frac{\hat{B}_g}{B_m} \tag{3}$$

The values in Table 4 show that radial magnetization provides better use of the magnet weight. Nevertheless, the main drawback to applying radial magnetization is its manufacturing process since a specific magnetic circuit with molds needs to be built. The baseline motor shown in Table 4 uses parallel magnetization [23], so it is opted to find a solution with parallel magnetization because the magnet unit cost is maintained for the same rotor structure since no change during the magnetization process is required.

In practical terms, as seen in Figure 7, the geometry is limited only to parallel or radial magnetization. Therefore, the proposed method requires splitting the banana, as seen in the baseline motor in Figure 1 and its model in Figure 4. Although this will increase the leakage due to the new ribs, it can also allow the implementation of parallel magnetization differently. The hypothesis is that since radial magnetization provides the highest $\hat{B}_{g1}$, there should be an optimum tilt angle that increases $\hat{B}_{g1}$ compared to the conventional parallel magnetization (straight as seen in Figure 7a) for the same magnet weight. Hence, getting the most out of the magnet weight with parallel magnetization in a given rotor structure.

So, $\hat{B}_{g1}$ is obtained for a sweep of tilt angles, $\alpha_1$ and $\alpha_2$, from 0° to 90° applied to each magnet, as seen in Figure 4. Table 5 shows the main results quantities of the sweep for $\hat{B}_{g1}$ in per unit, normalized over $\hat{B}_{g1}$ for radial magnetization (1.0934 T shown in the table, equivalent to one per unit) shows the resulting curve of the sweep for $\hat{B}_{g1}$ in per unit.

**Table 5.** Peak fundamental flux density result and corresponding tilt angles normalized to radial magnetization value.

| Magnetization Pattern | $\hat{B}_{g1}$ [*pu*] | $\alpha_1$ [°] | $\alpha_2$ [°] |
|---|---|---|---|
| $\hat{B}_{g1}$ maximum with a different angle | 0.99291 | 36 | 19.4 |
| $\hat{B}_{g1}$ maximum with same angle | 0.98067 | 29.4 | 29.4 |
| $\hat{B}_{g1}$ straight angle | 0.84588 | 0 | 0 |
| $\hat{B}_{g1}$ radial | | 1.0934 [T] | |

The remarks for the baseline motor from the results shown in Figure 8 and Table 5 are:

1. The maximum fundamental air gap flux density consists of a different tilt angle for each magnet ($\alpha_1$: 36° and $\alpha_2$: 19.4°), obtaining a 0.99291 per unit of the radial magnetization for this case study.
2. A second option is choosing the maximum air gap flux density that applies the same tilt angle to both magnets ($\alpha_1$: 29.4° and $\alpha_2$: 29.4°), leading to a slightly lower value than the maximum. In this case, 0.98067 per unit of the radial magnetization and the difference between the $\hat{B}_{g1}$ maximum is 0.01224 per unit.
3. Straight magnetization (initial parallel magnetization at zero degrees) provides the smallest value of the three options. In this case, 0.84588 per unit of the radial magnetization. This pattern is the typical way of applying parallel magnetization.

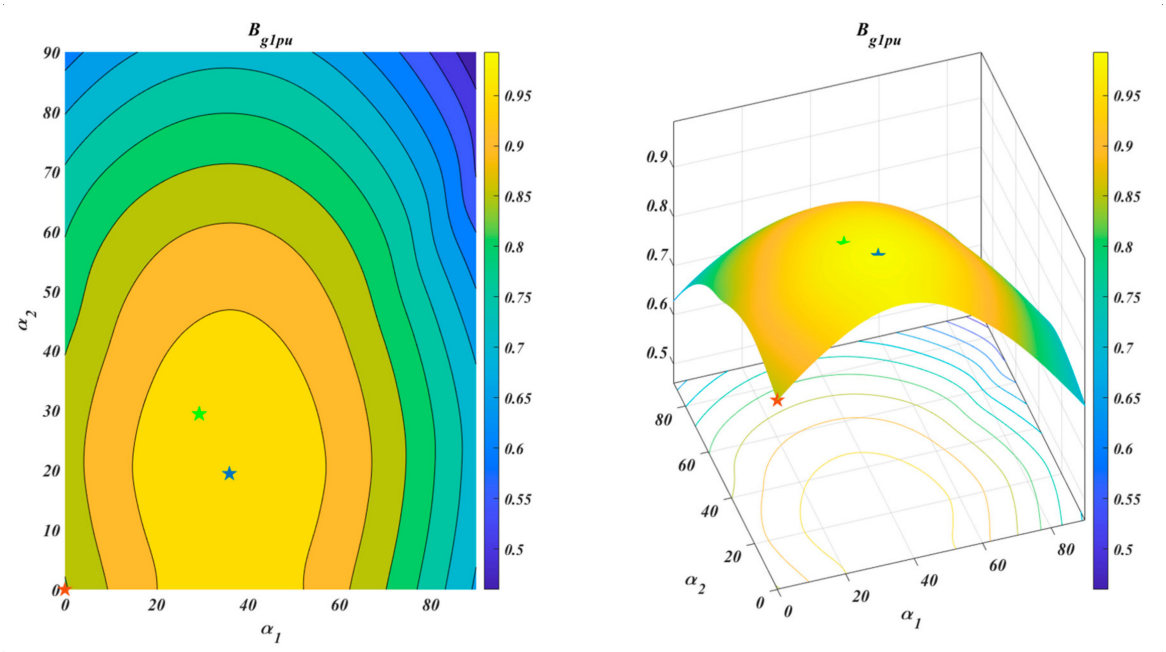


**Figure 8.** Peak fundamental harmonic air gap flux density for 0° to 90° tilt angles.

Figure 9a illustrates how to obtain the tilted desired pattern with parallel magnetization for the real magnet part. Figure 9b would illustrate the resulting magnetization pattern in the motor model if the magnet parts were magnetized in this way.

The solution is to tilt the magnet part to the desired angle (29.4° in this case), which provides the manufacturing advantage of continuing to use parallel magnetization (illustrated by the red arrow in Figure 9a). Thus, the magnet part is tilted instead of adjusting or changing the magnetization device. Therefore, keeping the same parallel magnetization device provides the advantage of avoiding extra investment in a different magnetization device, as explained in Section 1.

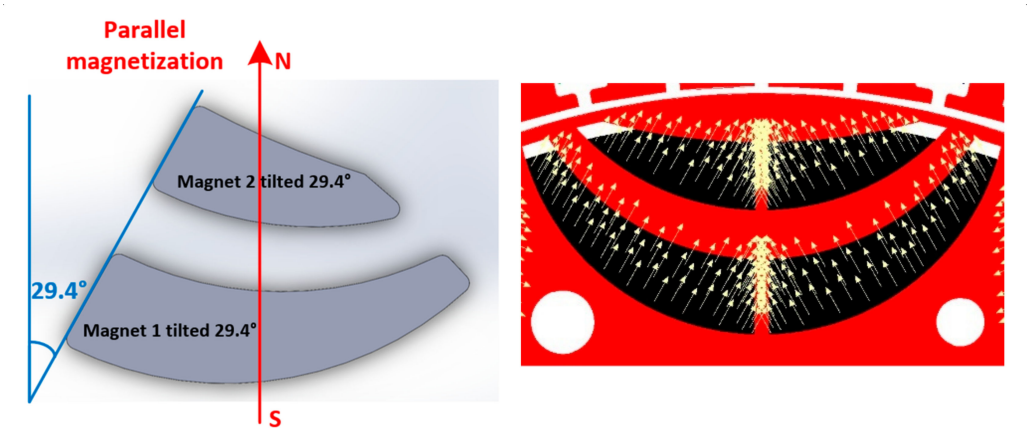


**Figure 9.** Tilting the magnet part within parallel magnetization to obtain the titled magnetization pattern. (**a**) Illustration how the real magnet part should be tilted within parallel magnetization; (**b**) View of the desired magnetization pattern in the motor model if magnetized as in (**a**).

From here onward, the same tilt angle pattern for both magnets is selected for two reasons. The first reason is the slight difference of 0.01224 per unit between $\hat{B}_{g1}$ maximum and the $\hat{B}_{g1}$ maximum with the same tilt angle option for both magnets. The second reason is that it could open the possibility of magnetizing both magnets simultaneously, as seen in Figure 9a. Figure 10 presents the flux density distribution and flux lines in FEM at no load and ambient temperature with the initial magnetization (straight at zero degrees) and the tilted magnetization with the same angle pattern.

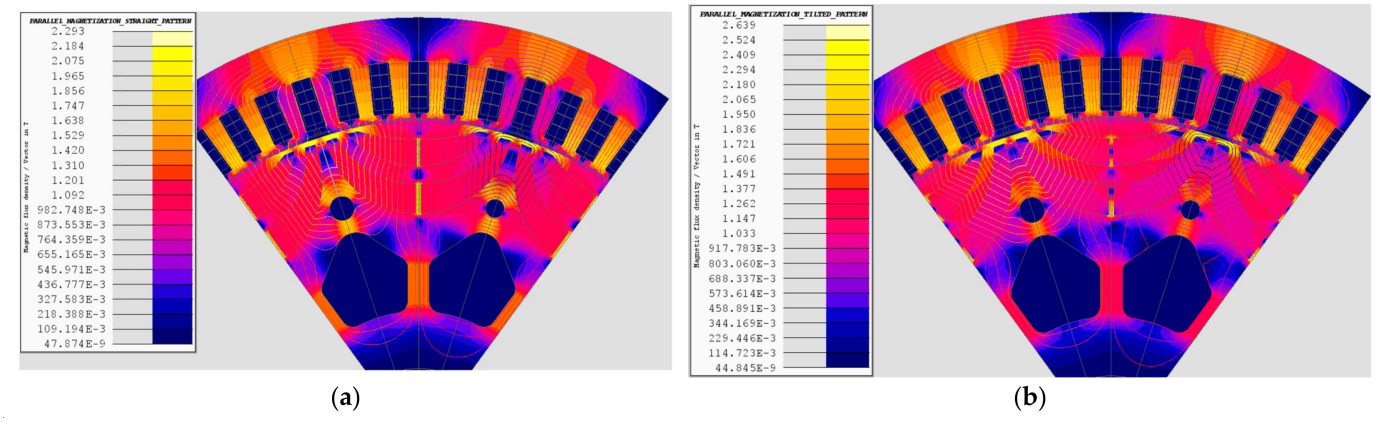


**Figure 10.** Baseline motor, no-load flux density distribution: (**a**) parallel magnetization: straight pattern; (**b**) parallel magnetization: tilted magnetization.

The performance comparison between the baseline motor model with straight magnetization and tilted magnetization with the same angle for both magnets is given in Figure 10. The performance comparison targets a similar thermal performance (winding and magnet temperatures), as shown in the same table.

Moreover, for this case study, a simple demagnetization analysis is carried out to check if there could be a risk of demagnetization at the operating temperature. The analysis is done by exporting the magnetic flux density and magnetic field of all geometric nodes within the magnet regions and comparing them against the BH curve of the magnet. In addition, all the nodes of each magnet were exported for each position in one electrical period. Figure 11 shows the results for both magnetization cases. It can be noticed that all points are on or above the magnet demagnetization curve. Therefore, it is concluded that no magnet is at risk of demagnetization at this temperature level.

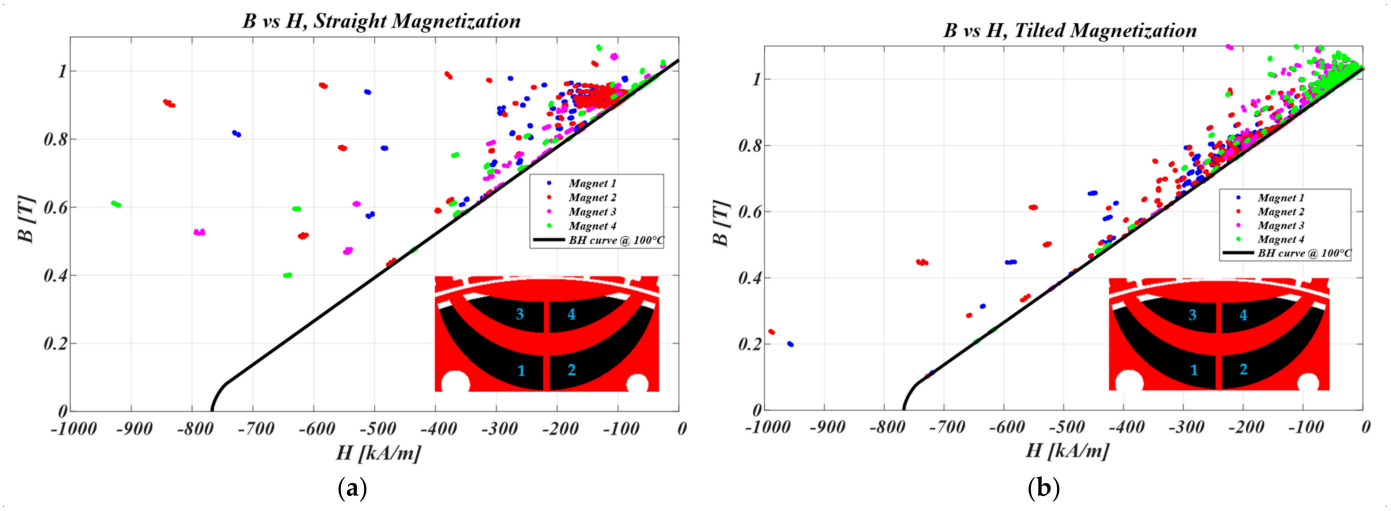


(**a**) (**b**)

**Figure 11.** Magnet nodes BH values for each position in one electrical period and magnet demagnetization curve at 100 °C. (**a**) Baseline motor BH values for straight magnetization; (**b**) Baseline motor BH values for tilted magnetization.

Finally, it is important to notice from Table 6 that the tilted magnetization pattern with the same tilt angle results in a machine with 7.14% more output torque than the baseline motor with the conventional parallel magnetization (straight magnetization) for the same thermal performance. Therefore, this higher magnetic loading opens the possibility of reducing the magnet weight. So, to satisfy the requirements Table 3 in Section 2, the following section shows the workflow followed to obtain a less rare-earth motor using tilted magnetization.

**Table 6.** Performance comparison between straight and tilted magnetization for the baseline motor model of Figures 1 and 4.

| Parameter | Unit | Straight Magnetization | Tilted Magnetization |
|---|---|---|---|
| Mechanical torque | Nm | 39.34 | 42.15 |
| Speed | RPM | 2400 | 2400 |
| Efficiency | % | 93.11 | 93.4 |
| Torque ripple | % | 6.7 | 10.0 |
| Winding temperature | °C | 133 | 134.6 |
| Magnet temperature | °C | 100.3 | 101.2 |
| Tilt angles | ° | 0 | 29.4 |
| Magnet weight | kg | 1.3098 | 1.3098 |
| Electromagnetic torque | Nm | 39.40 | 42.21 |
| Current | A | 109.77 | 109.86 |
| Current angle | ° | 29.86 | 24.82 |
| Copper losses | W | 603.46 | 607.09 |
| Iron losses | W | 114.25 | 127.34 |
| Mechanical losses | W | 14.17 | 14.17 |
| Input active power | W | 10,620.1 | 11,343.3 |
| Input reactive power | VAR | 2785.43 | 2098.36 |

## 4. Workflow to Obtain the Motor Electromagnetic Design Candidate

The contribution of this paper was described in Section 3, which demonstrates that tilted magnetization for the same motor structure (same magnet weight) provides better performance than the conventional application of parallel magnetization (straight) but with the advantage of still using parallel magnetization. Accordingly, this makes possible a reduction of magnet weight in a motor for the same motor performance. Therefore, this section aims to obtain a motor candidate with less rare-earth with tilted magnetization.

The finding in Section 3 that tilted magnetization increased the baseline motor performance would allow the optimization of the magnet geometry in the rotor for the same stator. Nevertheless, in this use case study, the objective is to obtain a new design candidate that could significantly reduce the magnet weight using tilted magnetization for the same performance. Therefore, it is opted to optimize both stator and rotor. This section reports the implemented route in a systematic approach.

From Section 3, parallel magnetization could be used better than its conventional application in two ways. One way is by using an optimum angle for each magnet and the other way is choosing the maximum that uses the same tilt angle. In any case, the computational time spent on finding the tilt angle is high, specific for this case study in FEM took around four hours, which is too high for an optimization iteration process within an acceptable time. However, based on the previous results (in Table 5), it is noticed that the difference between radial and the $\hat{B}_{g1}$ maximum point is 0.709%. The difference between the radial and the second option using the same angle is 1.933%.

Therefore, radial magnetization is used in the optimization process to facilitate and reduce computational time in iterations. Afterward, the tilt angles can be searched to obtain the final electromagnetic design with less rare-earth for the same baseline motor performance. A predetermined MOGA algorithm is used for the rotor optimization from the commercial software Altair HyperStudy 2020. Although different solution routes could have been taken, the workflow followed is devised to accomplish the objective of a less-rare earth electromagnetic design candidate satisfying the requirements of Table 3 and at the same time, intending it could serve as a guideline to the reader.

The main processes carried out to obtain the less rare-earth motor candidate can be seen in Figure 12 and more details about the first two actions are given in the activity diagrams in Figures 13 and 14.

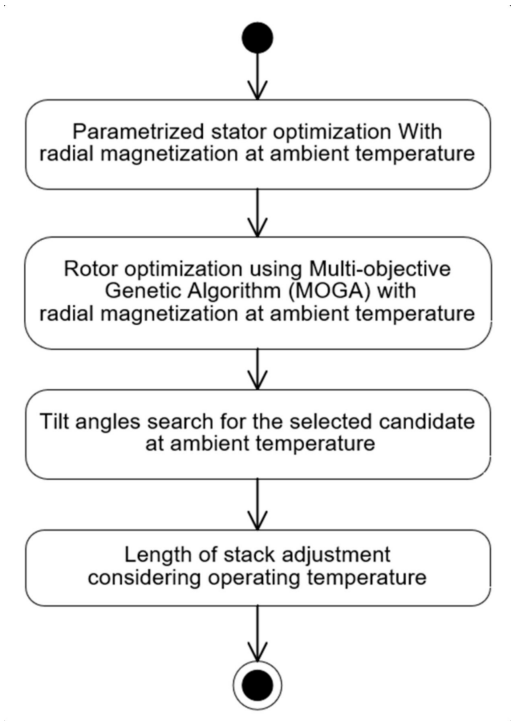


**Figure 12.** Optimization workflow.

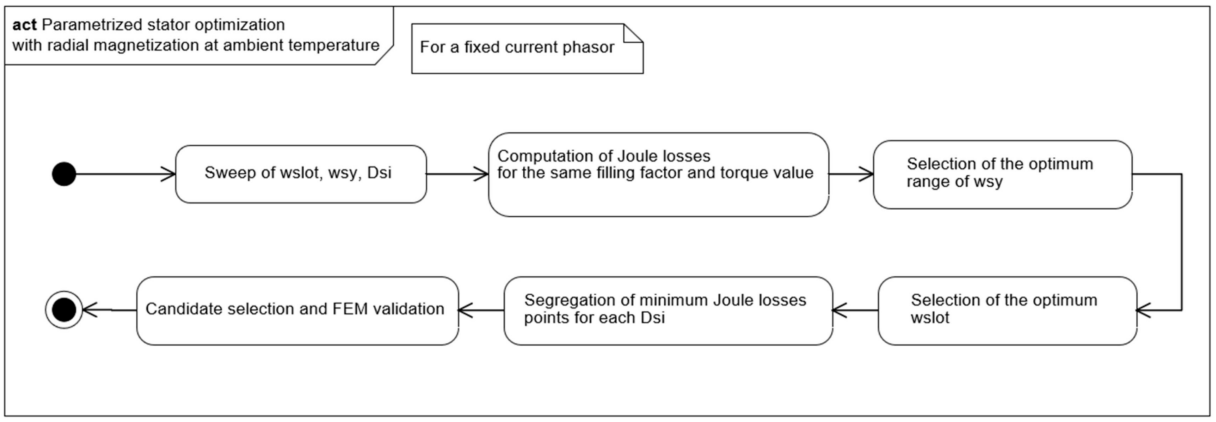


**Figure 13.** Stator optimization activity diagram.

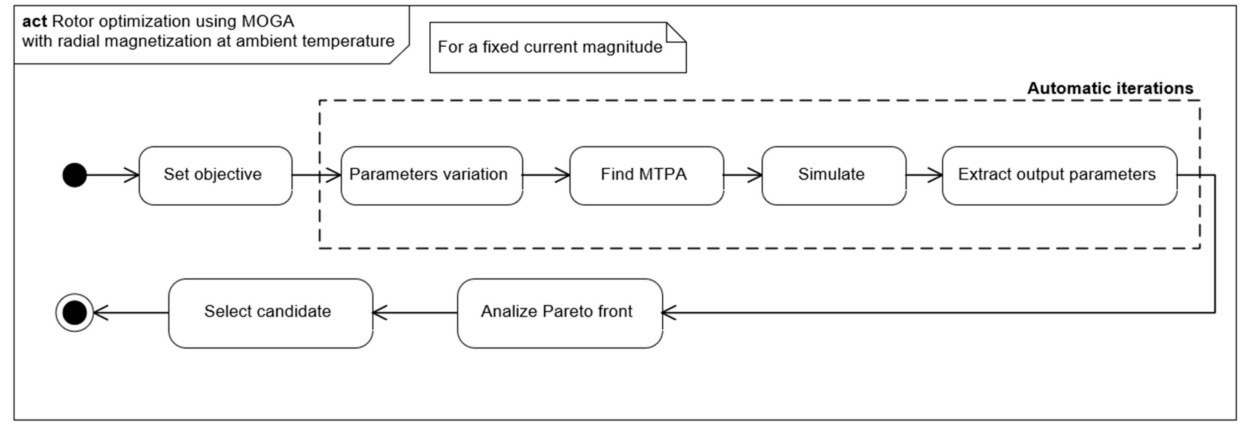


**Figure 14.** Rotor optimization activity diagram.

In the first stage, a parametrized stator optimization takes place, keeping the same magnet shape and weight. Therefore, the minimum $D_{si}$ is limited to the one that can accommodate the initial magnet weight and shape. The reason for a parametrized optimization for the stator is to speed up the whole optimization process.

The starting point is to simulate a given range of values for a fixed current phasor and speed for the parameters $w_{slot}$, $w_{sy}$ and $D_{si}$ (all parameters shown in Figure 4 and the nomenclature section) in FEM. Later, the computation of DC Joule losses is carried out with the results, keeping the same filling factor for all geometry cases and targeting the initial torque value as the reference. For this, Equation (4) is used, it is true that by applying Equation (4), linearity is assumed, but for this reason, a further step is to validate the selected candidate in FEM. However, since the range selected for the stator parameters does not include wide steps from the reference value, the expected results are presumed close enough.

$$P_{Joule} = 3 \cdot R_{DC} \cdot \left( \frac{I_{s\_ref}}{\tau_{ratio}} \right)^2, \text{ where } \tau_{ratio} = \frac{\tau}{\tau_{ref}} \tag{4}$$

Next, the Joule losses versus $w_{sy}$ versus $w_{slot}$ for each $D_{si}$ is analyzed from where an optimum range of $w_{sy}$ is selected. Afterward, for each $w_{sy}$ (selected), the Joule losses versus $w_{slot}$ for all $D_{si}$ are analyzed from where the minimum points are segregated. Finally, the minimum Joule losses for each $D_{si}$ are plotted from which one candidate was selected. The selected candidate also considered other mechanical aspects, such as the distance between poles and the distance between the magnet layers. However, these mechanical aspects are out of the scope of this paper. Figure 15 shows the results and the plot of minimums with

the selected candidate highlighted. The selected candidate operating point was validated in FEM, resulting in an output torque variation of −0.32%.

| $P_{Joule}$ Decrease [%] | $Dsi$ [mm] | $wsy$ [mm] | $wslot$ [mm] | $wd^{i}_{bottom}$ [mm] | $DistPole$ [mm] | $Ratio$ [Dsi/Dso] | $J_{peak}$ [$A/mm^2$] | Est. Joule Losses [W] |
|---|---|---|---|---|---|---|---|---|
| Ref. | 123 | 8.23 | 3.86 | 2.716 | 2.076 | 0.7640 | 13.3547 | 360.9162 |
| 14.910 | 118 | 6.5 | 4 | 2.314 | 0.4802 | 0.7329 | 9.8156 | 307.1036 |
| 14.4771 | 118.5 | 6.5 | 4 | 2.34 | 0.6405 | 0.7360 | 9.9173 | 308.6658 |
| 13.9745 | 119 | 6.5 | 4 | 2.366 | 0.8007 | 0.7391 | 10.0258 | 310.4800 |
| 13.3981 | 119.5 | 6.5 | 4 | 2.392 | 0.9607 | 0.7422 | 10.1414 | 312.5601 |
| 12.7345 | 120 | 6.5 | 4 | 2.418 | 1.12 | 0.7453 | 10.2651 | 314.9554 |
| 11.9996 | 120.5 | 6.5 | 4 | 2.445 | 1.28 | 0.7484 | 10.3963 | 317.6078 |
| 11.1854 | 121 | 6.5 | 4 | 2.471 | 1.44 | 0.7515 | 10.5356 | 320.5463 |
| 10.2919 | 121.5 | 6.5 | 4 | 2.497 | 1.599 | 0.7546 | 10.6833 | 323.7710 |
| 9.3222 | 122 | 6.5 | 4 | 2.523 | 1.758 | 0.7578 | 10.8394 | 327.2707 |
| 8.2727 | 122.5 | 6.5 | 4 | 2.549 | 1.917 | 0.7609 | 11.0045 | 331.0588 |
| 7.1407 | 123 | 6.5 | 4 | 2.576 | 2.076 | 0.7640 | 11.1789 | 335.1443 |
| 5.9147 | 123.5 | 6.5 | 4 | 2.602 | 2.234 | 0.7671 | 11.3636 | 339.5691 |
| 4.5816 | 124 | | | | | | | |
| 3.1339 | 124.5 | | | | | | | |
| 1.5706 | 125 | | | | | | | |
| -0.1021 | 125.5 | | | | | | | |
| -1.8795 | 126 | | | | | | | |
| -31.4176 | 132 | | | | | | | |

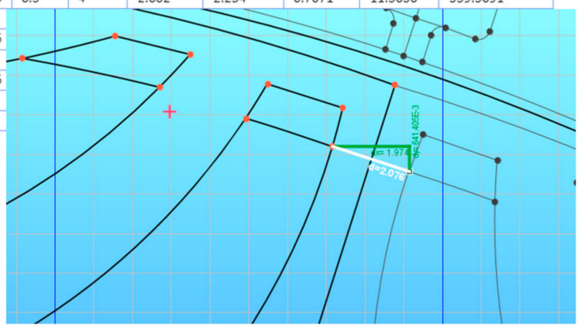

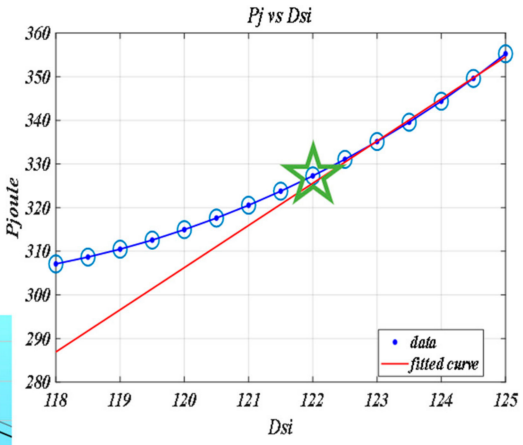


**Figure 15.** (**Left**) Minimum Joule losses for each $D_{si}$ in the stator optimization results. (**Middle**) Sketch showing the distance between magnet poles for the reference case. (**Right**) Plot of minimum Joule losses for each $D_{si}$ and the selected candidate.

The rotor optimization is the second stage of Figure 12 and it is executed at room temperature (20 °C) using a multi-objective genetic algorithm (MOGA) included in the software Altair HyperStudy 2020.1. The treated rotor parameters are shown in Figure 4 and Equation (5). The stack length is kept as 66 mm for the optimization process. So first, the objective is set, as seen in Equation (5). Then, the automatic iteration process in Figure 14 consists of finding the Maximum Torque per Ampere (MTPA) point using the fifth FEM-coupled algorithm from [24], done for a fixed current magnitude and each variation of parameters. Once the MTPA point is found, the point is simulated in FEM and the output parameters are extracted.

$$\begin{aligned} &\text{Objective,} \\ &Maximize: \ \tau([x_{parameter}]) \\ &Minimize: \ W_m([x_{parameter}]) \\ &where\ x_{parameter} = [l_{m1}, l_{m2}, Dre_{Shape}, R_{l1}, R_{h1}, R_{l2}, R_{h2}, \beta_1, \beta_2] \\ &\text{Constraints,} \\ &\tau_{ripple} \leq 6.7\% \end{aligned} \tag{5}$$

The optimization results at room temperature are shown in Figure 16. The Pareto front and the selected candidate are highlighted in the figure. In addition, images of the magnet geometries variations in three sections of the Pareto front (bottom, middle, top). It is worth remarking again that the Pareto front shown in Figure 16 is for radial magnetization. However, extensive computational time to find the optimal tilt angle for each iteration is avoided by doing this and since the final results satisfy the requirements of Table 3, the process was established as acceptable. Going to the right on the curve (Figure 16), it can be noticed that the magnet layers approach each other. Therefore, the selected candidate from the Pareto front also involves mechanical criteria for the distance between magnet poles and magnet layers. The torque was chosen to be maximized (while minimizing the magnet weight) and not constrained in order to have the additional degree of freedom of

stack length reduction. In addition, less magnet weight, stack length reduction provides additional material reduction, such as less copper and electric steel.

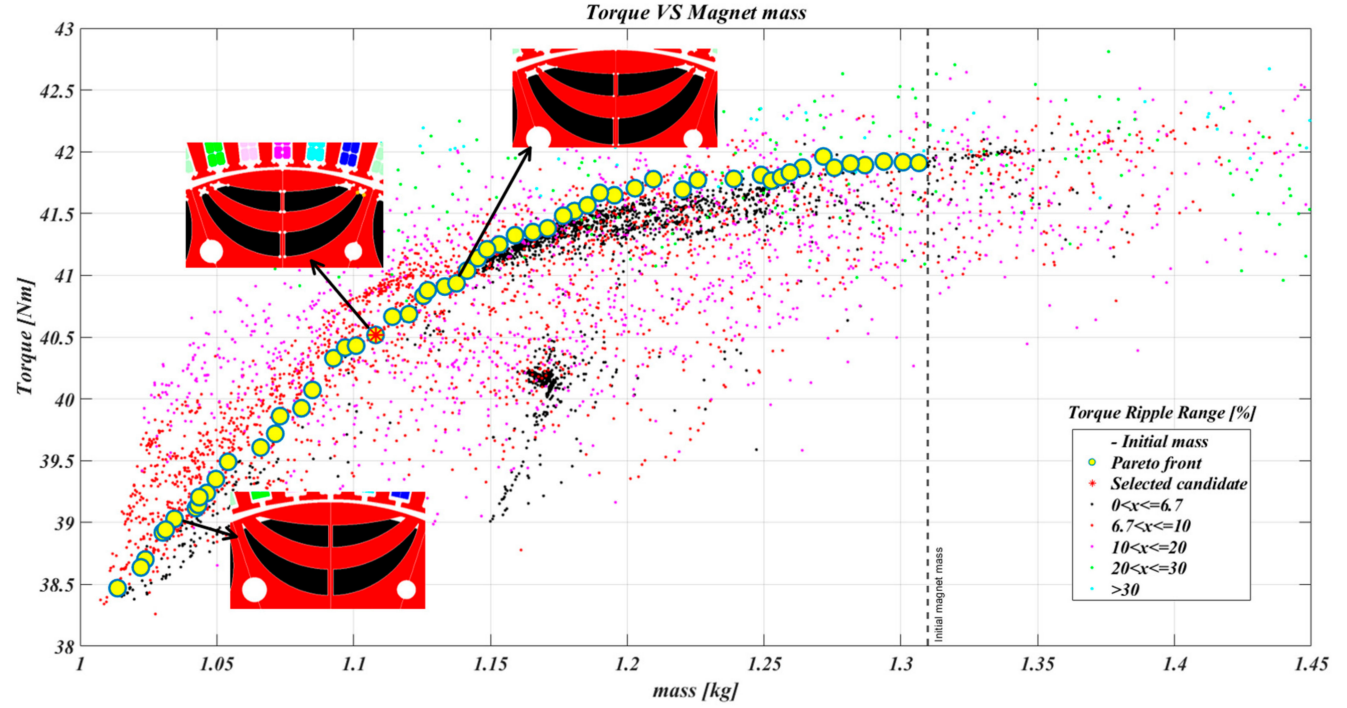


**Figure 16.** Rotor optimization process results and Pareto front.

The next stage of Figure 12 is to find the tilt angles. Following the same process mentioned in Section 3, the angles and the fundamental flux density values are shown in Table 7.

**Table 7.** Peak fundamental flux density result and corresponding tilt angles.

| Magnetization Pattern | $\hat{B}_{g1}$ $[pu]$ | $\alpha_1$ [°] | $\alpha_2$ [°] |
|---|---|---|---|
| $\hat{B}_{g1}$ maximum with a different angle | 0.99694 | 37.4 | 21.5 |
| $\hat{B}_{g1}$ maximum with same angle | 0.98727 | 28.6 | 28.6 |
| $\hat{B}_{g1}$ straight angle | 0.88292 | 0 | 0 |
| $\hat{B}_{g1}$ radial | | 0.98628 [T] | |

Finally, using the angle values for the maximum flux density with the same tilt angles, the stack length is adjusted for the same torque and speed operating point until reaching the baseline motor's thermal performance (copper and magnet temperature). In other words, iterations for different stack lengths were executed until the temperatures were considered close enough. Figure 17 shows the 2D appearance of the optimized motor, which can be compared with the initial geometry shown in Figures 4 and 10a.

Table 8 shows the final performance comparison between the baseline motor with straight magnetization and the optimized one. The optimized motor has a 21.82% less magnet weight than the baseline motor. Therefore, achieving the objective of a less rare-earth electromagnetic design motor candidate that satisfies the requirements in Table 3.

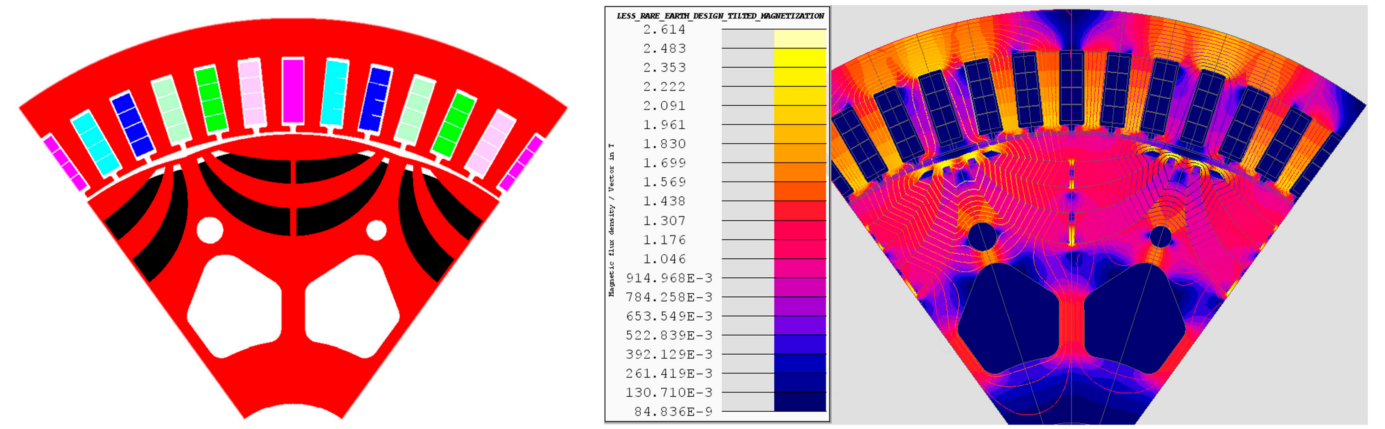


**Figure 17.** Less rare-earth motor selected candidate (**a**) Motor 2D view; (**b**) No-load flux density distribution.

**Table 8.** Performance comparison of same operating point performance between the baseline motor of Figure 1 with parallel magnetization and the selected candidate with tilted magnetization.

| Parameter | Unit | Baseline Motor with Parallel Magnetization | Optimized Motor with Tilted Magnetization |
|---|---|---|---|
| Mechanical torque | Nm | 39.34 | 39.30 |
| Speed | RPM | 2400 | 2400 |
| Efficiency | % | 93.11 | 93.27 |
| Torque ripple | % | 6.7 | 3.225 |
| Winding temperature | °C | 133 | 132.8 |
| Magnet temperature | °C | 100.3 | 98.4 |
| Tilt angles | ° | 0 | 28.6 |
| Stack length | mm | 66 | 61 |
| Magnet weight | kg | 1.3098 | 1.02406 |
| Magnet weight decrease | % | - | 21.82 |
| Electromagnetic torque | Nm | 39.40 | 39.35 |
| Current | A | 109.77 | 123.66 |
| Current angle | ° | 29.86 | 25.05 |
| Copper losses | W | 603.46 | 583.49 |
| Iron losses | W | 114.25 | 116.00 |
| Mechanical losses | W | 14.17 | 12.88 |
| Input active power | W | 10,620.1 | 10,588.28 |
| Input reactive power | VAR | 2785.43 | 2547.21 |

Finally, similar to Section 3, Figure 18 shows that the BH values of the magnet nodes are on or above the magnet demagnetization curve, so there is no risk of demagnetization for the working temperature.

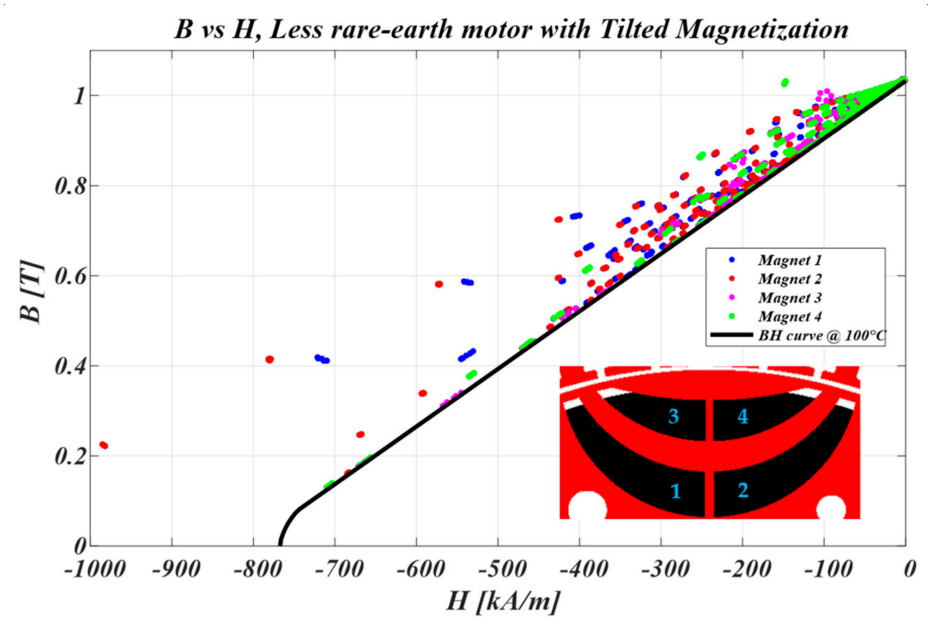


**Figure 18.** Less rare–earth motor candidate BH values and magnet demagnetization curve at 100 °C.

## 5. Discussion

Banana-shaped permanent magnet motors typically use parallel magnetization (straight pattern). Between parallel and radial magnetization, radial provides a higher air-gap flux density. However, parallel magnetization is typically used in motor design to avoid extra manufacturing costs that may not compensate for the performance improvement. This paper proposed an alternative to the design process. The process applies tilted magnetization to obtain a less rare-earth motor candidate with banana-shaped topologies using only electromagnetic design. Initially, tilted magnetization was applied to the baseline motor model, increasing the output torque by 7.14%. This increase of torque due to a higher magnetic loading demonstrates that tilted magnetization is a better option than the straight pattern (zero degrees) when designing banana-shaped motors because it provides better use of the magnet weight.

Two options of tilt angles were proposed either the maximum point consisting of different tilt angles for each magnet layer or the maximum with the same tilt angle. Even though there is a slight decrease of 1–2% of the fundamental air gap flux density compared to radial magnetization, it is still an excellent alternative to radial magnetization because it presents the manufacturing advantage of keeping the conventional parallel magnetization. So, instead of building a specialized mold as in radial, it is only required to tilt the magnet part to get the desired pattern.

The application of the presented workflow resulted in a motor candidate that achieved a magnet weight reduction of 21.82%, demonstrating that titled magnetization is an excellent alternative in the electromagnetic design of banana-shaped motors. This fact has not been published to the authors' understanding, making it an innovative solution for this topology.

## 6. Conclusions and Future Work

Compared to the conventional application of parallel magnetization, the tilted magnetization pattern improves the motor performance for the same magnet weight. So, it allows magnet weight reduction for the same motor performance for new designs.

Tilted magnetization still uses the conventional parallel magnetization, but the magnet part should be tilted to get the desired pattern. The maximum fundamental air gap flux density consists of a different tilt angle for each magnet. A second option is choosing the maximum air gap flux density that applies the same tilt angle to both magnets, leading to a

slightly lower value than the absolute maximum, but it opens the possibility of magnetizing both magnets simultaneously.

In this case study, the optimized motor has a 21.82% less magnet weight than the baseline motor. Therefore, achieving the objective of a less rare-earth electromagnetic design. Future work should analyze different manufacturing technologies to develop sintered banana-shaped magnets. Additionally, a combination of Cerium substitution to any manufacturing technology with this topology could result in even less rare-earth designs.

Moreover, future work may further research the impact of demagnetization with tilted magnetization at higher temperatures. Particular attention should be paid to the demagnetizing limit on built electric machines that would like to apply tilted magnetization in current products.

**Author Contributions:** G.U. and J.P. conceived the research; G.U. and C.A.R. designed the research; C.A.R. developed the tilted design process and wrote the manuscript; G.U., J.P. and F.G. reviewed and validated the work; X.B. validated the work. All authors have read and agreed to the published version of the manuscript.

**Funding:** This activity has received funding from the European Institute of Innovation and Technology (EIT), a body of the European Union, under the Horizon 2020, the EU Framework Programme for Research and Innovation under grant agreement no. 19120 LowReeMotors rare-earth reduction in high performance permanent magnet electric machines. https://www.lowreemotors.eu/ (accessed on 20 February 2022).

**Institutional Review Board Statement:** Not applicable.

**Informed Consent Statement:** Not applicable.

**Conflicts of Interest:** The authors declare no conflict of interest.

## Nomenclature

| | |
|---|---|
| $\hat{B}_g$ | Peak air gap flux density |
| $\hat{B}_{g1}$ | Peak fundamental harmonic air gap flux density |
| $B_m$ | Magnet flux density operating point |
| $H_m$ | Magnet field operating point |
| $B_r$ | Magnet remanence |
| $S_m$ | Magnet surface area |
| $S_g$ | Air gap surface area |
| $g$ | Air gap length |
| $l_m$ | Magnet length |
| $C_{\varphi_S}$ | Flux concentration factor with surface ratio |
| $C_{\varphi_B}$ | Flux concentration factor with flux density ratio |
| $\mu_r$ | Magnet relative permeability |
| $w_{slot}$ | Slot width |
| $w_{sy}$ | Stator yoke width |
| $D_{si}$ | Stator inner diameter |
| $P_{Joule}$ | Joule losses |
| $R_{DC}$ | DC resistance |
| $I_{s\_ref}$ | Current magnitude reference |
| $\tau_{ratio}$ | Torque ratio |
| $\tau$ | Torque |
| $\tau_{ref}$ | Reference Torque |
| $W_m$ | Magnet weight |
| $l_{m1}$ | Magnet length layer 1 |
| $l_{m2}$ | Magnet length layer 2 |
| $Dre_{Shape}$ | Rotor outer diameter pole span |

| | |
|---|---|
| $R_{l1}$ | Magnet lower radius layer 1 |
| $R_{h1}$ | Magnet upper radius layer 1 |
| $R_{l2}$ | Magnet lower radius layer 2 |
| $R_{h2}$ | Magnet upper radius layer 2 |
| $\beta_1$ | Magnet span layer 1 |
| $\beta_2$ | Magnet span layer 2 |
| $\tau_{ripple}$ | Torque ripple |
| $PC$ | Permeance coefficient |

## References


1. Rietmann, N.; Hügler, B.; Lieven, T. Forecasting the trajectory of electric vehicle sales and the consequences for worldwide $CO_2$ emissions. *J. Clean. Prod.* **2020**, *261*, 121038. [CrossRef]
2. Watari, T.; Nansai, K.; Nakajima, K. Review of critical metal dynamics to 2050 for 48 elements. *Resour. Conserv. Recycl.* **2020**, *155*, 104669. [CrossRef]
3. Kim, H.S.; You, Y.M.; Kwon, B. Il Rotor shape optimization of interior permanent magnet BLDC motor according to magnetization direction. *IEEE Trans. Magn.* **2013**, *49*, 2193–2196. [CrossRef]
4. Hayakawa, K.; Sanada, M.; Morimoto, S.; Inoue, Y. Evaluation of IPMSMs with concentrated windings using powder magnets for high torque. In Proceedings of the International Conference on Power Electronics and Drive Systems, Kitakyushu, Japan, 22–25 April 2013; pp. 735–740.
5. Abad, V.; Sagredo, J.; Gonzalez, J. FEA Analysis and Optimization of Rotor Models in Permanent-Magnet Synchronous Motors fitted with Bonded Rare-Earth Magnets. In Proceedings of the International Conference on Renewable Energies and Power Quality (ICREPQ' 19), Tenerife, Spain, 10–12 April 2019; pp. 37–42.
6. HSMAG: Multipole Radial Ring Magnets. Available online: https://www.hsmagnets.com/permanent-magnets/multipole-radial-ring-magnets/ (accessed on 15 November 2021).
7. LowReeMotors. Available online: https://www.lowreemotors.eu/ (accessed on 23 December 2021).
8. Wang, S.; Youn, D.; Moon, H.; Kang, J. Topology optimization of electromagnetic systems considering magnetization direction. *IEEE Trans. Magn.* **2005**, *41*, 1808–1811. [CrossRef]
9. Liu, H.C.; Kim, H.W.; Jang, H.K.; Jang, I.S.; Lee, J. Ferrite PM Optimization of SPM BLDC Motor for Oil-Pump Applications According to Magnetization Direction. *IEEE Trans. Appl. Supercond.* **2020**, *30*, 1–5. [CrossRef]
10. Yu, D.; Huang, X.; Zhang, X.; Zhang, J.; Lu, Q.; Fang, Y. Investigation the optimum performance of the surface-mounted PMSM under different magnetization patterns. *J. Phys. Conf. Ser.* **2020**, *1432*, 012005. [CrossRef]
11. Hoseinpour, A.; Mardaneh, M.; Rahideh, A. Investigation of the effects of different magnetization patterns on the performance of series hybrid excitation synchronous machines. *Prog. Electromagn. Res. M* **2018**, *64*, 109–121. [CrossRef]
12. Petkovska, L.; Cvetkovski, G.V.; Lefley, P. Study for performance characteristics of surface permanent magnet motor at various magnetization patterns. *COMPEL-Int. J. Comput. Math. Electr. Electron. Eng.* **2016**, *35*, 1910–1924. [CrossRef]
13. Ferraris, L.; Ferraris, P.; Poskovic, E.; Tenconi, A. Evaluation of the magnetization direction effects on ferrite PM brushless fractional machines. In Proceedings of the IECON 2012—38th Annual Conference on IEEE Industrial Electronics Society, Montreal, QC, Canada, 25–28 October 2012; pp. 6194–6199. [CrossRef]
14. Ferraris, L.; Ferraris, P.; Pošković, E.; Tenconi, A. Comparison between parallel and radial magnetization in PM fractional machines. In Proceedings of the ECON 2011—37th Annual Conference of the IEEE Industrial Electronics Society, Melbourne, Australia, 7–10 November 2011; pp. 1776–1782. [CrossRef]
15. Oh, S.; Min, S.; Hong, J.P. Air gap flux density waveform design of surface-mounted permanent magnet motor considering magnet shape and magnetization direction. *IEEE Trans. Magn.* **2013**, *49*, 2393–2396. [CrossRef]
16. Kim, H.; Kwon, J.; Kwon, B. Investigation of slot-pole combinations on IPM BLDC motor considering magnetization direction. *Int. J. Appl. Electromagn. Mech.* **2019**, *59*, 865–872. [CrossRef]
17. Kim, H.S.; Kwon, B. Il Optimal design of motor shape and magnetisation direction to obtain vibration reduction and average torque improvement in IPM BLDC motor. *IET Electr. Power Appl.* **2017**, *11*, 378–385. [CrossRef]
18. Nobahari, A.; Mosavi, M.R.; Vahedi, A. Optimal shaping of non-conventional permanent magnet geometries for synchronous motors via surrogate modeling and multi-objective optimization approach. *Iran. J. Electr. Electron. Eng.* **2020**, *16*, 114–121. [CrossRef]
19. Ho, S.L.; Li, H.L.; Fu, W.N. A post-assembly magnetization method of direct-start interior permanent magnet synchronous motors and its finite-element analysis of transient magnetic field. *IEEE Trans. Magn.* **2012**, *48*, 3238–3241. [CrossRef]
20. Zheng, P.; Liu, Y.; Wang, Y.; Cheng, S. Magnetization analysis of the brushless DC motor used for hybrid electric vehicle. In Proceedings of the 2004 12th Symposium on Electromagnetic Launch Technology, Snowbird, UT, USA, 25–28 May 2004; Volume 41, pp. 542–545. [CrossRef]
21. Dorrell, D.G.; Hsieh, M.F.; Hsu, Y.C. Post assembly magnetization patterns in rare-earth permanent-magnet motors. *IEEE Trans. Magn.* **2007**, *43*, 2489–2491. [CrossRef]

22. Wang, Q.; DIng, H.; Zhang, H.; Lv, Y.; Guo, H.; Li, L. Study of a Post-Assembly Magnetization Method of a V-Type Rotor of Interior Permanent Magnet Synchronous Motor for Electric Vehicle. *IEEE Trans. Appl. Supercond.* **2020**, *30*, 1–5. [CrossRef]
23. Li, Z. Electrical Radial Flux Machine Design Focusing on Magnet Recycling and Reuse: Application to Hybrid or Electric Vehicles. Ph.D. Dissertation, Université Grenoble Alpes, Grenoble, France, 2019.
24. Rivera, C.; Poza, J.; Ugalde, G.; Almandoz, G. Field Weakening Characteristics Computed with FEM-Coupled Algorithms for Brushless AC Motors. *Energies* **2018**, *11*, 1288. [CrossRef]
25. Hanselman, D.C. *Brushless Permanent Magnet Motor Design*; The Writers' Collective: Toronto, ON, USA, 2006; ISBN 10-1-881855-15-5.